


## First measurement of differential cross sections and photon beam asymmetries for photoproduction of the $f_0(980)$ meson decaying into $\pi^0\pi^0$ at $E_\gamma < 2.4$ GeV

N. Muramatsu <sup>1,2</sup>, S. K. Wang,<sup>2</sup> Q. H. He,<sup>2</sup> J. K. Ahn,<sup>3</sup> W. C. Chang,<sup>4</sup> J. Y. Chen,<sup>5</sup> M. L. Chu,<sup>4</sup> S. Daté,<sup>6,7</sup> T. Gogami,<sup>8</sup> H. Goto,<sup>7</sup> H. Hamano,<sup>7</sup> T. Hashimoto,<sup>7</sup> K. Hicks,<sup>9</sup> T. Hiraiwa,<sup>10</sup> Y. Honda,<sup>1</sup> T. Hotta,<sup>7</sup> H. Ikuno,<sup>7</sup> Y. Inoue,<sup>1</sup> T. Ishikawa,<sup>7</sup> I. Jaegle,<sup>11</sup> J. M. Jo,<sup>3</sup> Y. Kasamatsu,<sup>7</sup> H. Katsuragawa,<sup>7</sup> S. Kido,<sup>1</sup> Y. Kon,<sup>7</sup> S. Masumoto,<sup>12</sup> Y. Matsumura,<sup>1</sup> M. Miyabe,<sup>1</sup> K. Mizutani,<sup>11</sup> T. Nakamura,<sup>13</sup> T. Nakano,<sup>7</sup> T. Nam,<sup>14</sup> M. Niiyama,<sup>15</sup> Y. Nozawa,<sup>16</sup> Y. Ohashi,<sup>6,7</sup> H. Ohnishi,<sup>1</sup> T. Ohta,<sup>16</sup> M. Okabe,<sup>1</sup> K. Ozawa,<sup>17</sup> C. Rangacharyulu,<sup>18</sup> S. Y. Ryu,<sup>7</sup> Y. Sada,<sup>1</sup> T. Shibukawa,<sup>12</sup> H. Shimizu,<sup>1</sup> R. Shirai,<sup>1</sup> K. Shiraishi,<sup>1</sup> E. A. Stokovsky,<sup>19,7</sup> Y. Sugaya,<sup>7</sup> M. Sumihama,<sup>13,7</sup> S. Suzuki,<sup>6</sup> S. Tanaka,<sup>7</sup> Y. Taniguchi,<sup>1</sup> A. Tokiyasu,<sup>1</sup> N. Tomida,<sup>20</sup> Y. Tsuchikawa,<sup>21</sup> T. Ueda,<sup>1</sup> T. F. Wang,<sup>22</sup> H. Yamazaki,<sup>23</sup> R. Yamazaki,<sup>1</sup> Y. Yanai,<sup>7</sup> T. Yorita,<sup>7</sup> C. Yoshida,<sup>1</sup> and M. Yosoi<sup>7</sup>  
(LEPS2/BGOegg Collaboration)

<sup>1</sup>Research Center for Electron Photon Science, Tohoku University, Sendai, Miyagi 982-0826, Japan

<sup>2</sup>Department of Nuclear Science and Technology, College of Materials Science and Technology, Nanjing University of Aeronautics and Astronautics, Nanjing 210016, China

<sup>3</sup>Department of Physics, Korea University, Seoul 02841, Republic of Korea

<sup>4</sup>Institute of Physics, Academia Sinica, Taipei 11529, Taiwan

<sup>5</sup>National Synchrotron Radiation Research Center, Hsinchu 30076, Taiwan

<sup>6</sup>Japan Synchrotron Radiation Research Institute (SPring-8), Sayo, Hyogo 679-5198, Japan

<sup>7</sup>Research Center for Nuclear Physics, Osaka University, Ibaraki, Osaka 567-0047, Japan

<sup>8</sup>Department of Physics, Kyoto University, Kyoto 606-8502, Japan

<sup>9</sup>Department of Physics and Astronomy, Ohio University, Athens, Ohio 45701, USA

<sup>10</sup>RIKEN SPring-8 Center, Sayo, Hyogo 679-5148, Japan

<sup>11</sup>Thomas Jefferson National Accelerator Facility, Newport News, Virginia 23606, USA

<sup>12</sup>Department of Physics, University of Tokyo, Tokyo 113-0033, Japan

<sup>13</sup>Department of Education, Gifu University, Gifu 501-1193, Japan

<sup>14</sup>Dalat Nuclear Research Institute, Dalat, Lam Dong 66106, Vietnam

<sup>15</sup>Department of Physics, Kyoto Sangyo University, Kyoto 603-8555, Japan

<sup>16</sup>Department of Radiology, The University of Tokyo Hospital, Tokyo 113-8655, Japan

<sup>17</sup>Institute of Particle and Nuclear Studies, High Energy Accelerator Research Organization (KEK), Tsukuba, Ibaraki 305-0801, Japan

<sup>18</sup>Department of Physics and Engineering Physics, University of Saskatchewan, Saskatoon SK S7N 5E2, Canada

<sup>19</sup>Laboratory of High Energy Physics, Joint Institute for Nuclear Research, Dubna, Moscow Region, 142281, Russia

<sup>20</sup>Center for Science Adventure and Collaborative Research Advancement (SACRA), Kyoto University, Kyoto 606-8502, Japan

<sup>21</sup>J-PARC Center, Japan Atomic Energy Agency, Tokai, Ibaraki 319-1195, Japan

<sup>22</sup>School of Physics, Beihang University, Beijing 100191, China

<sup>23</sup>Radiation Science Center, High Energy Accelerator Research Organization (KEK), Tokai, Ibaraki 319-1195, Japan



(Received 17 January 2023; accepted 28 March 2023; published 7 April 2023)

For the first time, differential cross sections and photon beam asymmetries were measured for the reaction  $\gamma p \rightarrow f_0(980)p \rightarrow \pi^0\pi^0 p$  by using a linearly polarized photon beam up to 2.4 GeV and a liquid hydrogen target. The  $f_0(980)$  photoproduction signal was clearly observed owing to the absence of contributions from vector-meson photoproduction. The results indicate the  $t$ -channel exchange of vector mesons as a mechanism of the  $f_0(980)$  photoproduction at  $E_\gamma \approx 2.1$  GeV, putting constraints on the nature of  $f_0(980)$ .

DOI: [10.1103/PhysRevC.107.L042201](https://doi.org/10.1103/PhysRevC.107.L042201)

The scalar meson  $f_0(980)$  has been attractive as a possible candidate of exotic non- $q\bar{q}$  states such as a  $K\bar{K}$  molecule and a tetraquark [1–4]. The measurement of differential cross sections and photon beam asymmetries in  $f_0(980)$  photoproduction is considered as one of the useful ways to understand its nature. For instance, a Regge model calculation with  $\rho$  and  $\omega$  exchange suggests that the differential cross section is sensitive to the strength of  $q\bar{q}$  and  $K\bar{K}$  components in the  $f_0(980)$  meson [5,6]. The  $t$ -channel vector-meson (natural

parity) exchange gives the photon beam asymmetry  $\Sigma$  of  $-1$  in the scalar meson photoproduction [7], and its magnitude decreases by the mixture of unnatural parity, which arises from axial-vector-meson exchange and rescattering diagrams, providing additional information about the  $f_0(980)$  nature. For the  $f_0(980)$  photoproduction, more theoretical calculations are available, for example, in Refs. [8,9].

Experimental observations of the  $f_0(980)$  photoproduction have been scarce and limited to the decay mode of  $f_0(980)$  into

$\pi^+\pi^-$  or  $K\bar{K}$  [10,11]. Differential cross sections were measured for the reaction  $\gamma p \rightarrow f_0(980)p \rightarrow \pi^+\pi^-p$  [10], but the  $\rho$ -meson photoproduction dominated the analysis sample. Thus, it was necessary to decompose  $S$ -wave pion pairs [e.g.,  $f_0(980)$ ] and  $P$ -wave pairs (e.g.,  $\rho$ ) by extracting moments. In contrast, the  $f_0(980)$  photoproduction with the  $f_0(980) \rightarrow \pi^0\pi^0$  decay is free of large contributions from the vector-meson photoproduction, as the vector mesons cannot decay by emission of a neutral pion pair. Additionally, so-called  $S$ - $P$  interference in the di-pion spectra due to the mixture of vector-meson photoproduction is not relevant with this decay mode. The present Letter focuses on the analysis of the  $\pi^0\pi^0p$  final state for the measurement of  $f_0(980)$  photoproduction off the proton, for the first time.

The analyzed data were collected in the BGOegg experiment conducted at the LEPS2 beamline of SPring-8 [12,13]. A linearly polarized photon beam tagged in the energy range of 1.3–2.4 GeV was produced via laser Compton scattering. The energies of individual photons were obtained by measuring recoil electron momenta at a tagging detector. The photon beam was incident on a 54 mm-long liquid hydrogen target in the experimental building. This target was surrounded by a high-resolution electromagnetic calorimeter comprising of 1320 BGO crystals. It covered the polar angles ( $\theta$ ) of  $24^\circ$ – $144^\circ$  with the division into 22 layers. In the region between the target and the calorimeter, 30 bars of plastic scintillators were arranged in a cylindrical shape for identifying whether a particle hitting the calorimeter was neutral or charged. The forward acceptance of  $\theta < 21^\circ$  was covered by a planar drift chamber for the detection of charged particles. Details of the experimental setup and its layout are described in Refs. [14–18].

The present analysis was performed by detecting all the final-state particles of the reaction  $\gamma p \rightarrow f_0(980)p \rightarrow \pi^0\pi^0p \rightarrow \gamma\gamma\gamma\gamma p$ . In the analyzed data, the integrated number of tagged beam photons reaches  $3.320 \times 10^{12}$  with the correction for dead times. Four  $\gamma$ s were detected by the large-acceptance calorimeter as neutral clusters, each of which contained several adjacent crystals with energy deposits from an electromagnetic shower. In order to avoid accepting accidental hits in the calorimeter as the final-state  $\gamma$ s, the minimum allowable cluster energy was set to 30 MeV and the hit timing difference between any two clusters was required to be less than 2 ns. A cluster having the largest-energy crystal (cluster core) at the most-forward or most-backward layer of the calorimeter was not treated as the final-state  $\gamma$  because of a large energy leak. A proton was detected as a charged cluster in the calorimeter or a straight track in the planar drift chamber. Only events with four neutral clusters and one charged particle hit were accepted in the further analysis.

Selected events were inspected by a kinematic fit with the four-momentum conservation for the double  $\pi^0$  photoproduction  $\gamma p \rightarrow \pi^0\pi^0p \rightarrow \gamma\gamma\gamma\gamma p$ . The initial state was defined by the measured beam energy and the proton rest mass. In the final state, the energy and direction of each  $\gamma$  were determined from the energy sum in a neutral cluster and the vector from the target center to the cluster core, respectively. The magnitude of a charged-particle momentum was not measured, but its emission angles were input into the kinematic fit with the assumption of a proton. Two sets of  $\gamma\gamma$  invariant masses

were both constrained to the nominal  $\pi^0$  mass [1]. There were three possibilities for making two  $\gamma\gamma$  combinations, so that the kinematic fit was repeated for all the possibilities to choose the best  $\chi^2$  case for a reconstructed event. Finally, the  $\chi^2$  probability was required to be greater than 2% to reduce backgrounds. The fitting result for the four-momenta of final-state particles was used to reconstruct  $\pi^0\pi^0$  and  $\pi^0p$  invariant masses to achieve better mass resolutions.

Events in the photon beam energy range below 1450 MeV were omitted by taking into account the production threshold for  $f_0(980)$ . Figure 1(a) shows the  $\pi^0p$  invariant mass distribution of remaining events after the kinematic fit. There are two entries per event because two  $\pi^0$  mesons are produced. Prominent peaks appear corresponding to  $\Delta(1232)$ ,  $N^*(1520)$ , and  $N^*(1650)$  resonances. The two higher-mass peaks may include other resonance contributions. In order to improve a  $f_0(980)$  signal-to-noise ratio, the final analysis sample was made with the upper side  $1\sigma$   $\Delta$  cut [ $M(\pi^0p) - 1232 > 50$  MeV], where only a lower momentum  $\pi^0$  was combined with a proton. About 133 000 events remain in the final sample.

Additionally,  $1\sigma$  cuts for  $N^*(1520)$  and  $N^*(1650)$  [ $|M(\pi^0p) - 1513| > 47$  MeV/ $c^2$  and  $|M(\pi^0p) - 1667| > 55$  MeV/ $c^2$ , respectively] were prepared for further systematic studies with background reduction. These  $N^*$  cuts also omit other resonance contributions in the observed peaks. Because the Breit-Wigner mass and width of the above  $N^*$ s were not well determined [1], they were obtained by fitting two Voigt functions (Breit-Wigner shapes convolved by the mass resolutions of about 11 MeV/ $c^2$ ) with a nonresonant component in the form of a second-order polynomial, as shown in Fig. 1(a). Here, only a high momentum  $\pi^0$  was combined with a proton for constructing the  $N^*(1650)$  cut. In contrast, the  $N^*(1520)$  cut was required for both of two  $\pi^0p$  combinations to make the condition efficient. The sample size decreases by half after the  $N^*$  cuts, causing large acceptance loss for signals.

Figures 1(b) and 1(c) show the  $\pi^0\pi^0$  invariant mass distributions for the higher ( $2110 < W < 2320$  MeV) and lower ( $1898 < W < 2110$  MeV) total-energy regions, respectively, in the case of no requirement of the  $N^*$  cuts. A peak corresponding to the  $f_0(980)$  signal is clearly seen without the influence of vector-meson photoproduction. In the present analysis, a Voigt function was simply used to represent the signal component, as done or indicated in recent papers [19–23]. So-called Flatté parametrization [24,25] was not adopted because of fitting difficulty arising from unknown background distributions. The mass resolution input into the Voigt function was estimated to be 13.3 and 9.3 MeV/ $c^2$  for Figs. 1(b) and 1(c), respectively, by using a Monte Carlo (MC) simulation based on GEANT4 [26] with implementation of a realistic setup. In Fig. 1(b), a Voigt function was fitted with a fourth-order polynomial background function. The mass and width of  $f_0(980)$  were obtained to be 964.5 and 84.4 MeV/ $c^2$ , respectively. For the lower  $W$  region, a similar fit was done by using the obtained Voigt function shape with the correction for the influence of production thresholds and making only the Breit-Wigner mass a free parameter. A fit in Fig. 1(c) resulted in the mass of 955.7 MeV/ $c^2$ . These fitting results were fixed

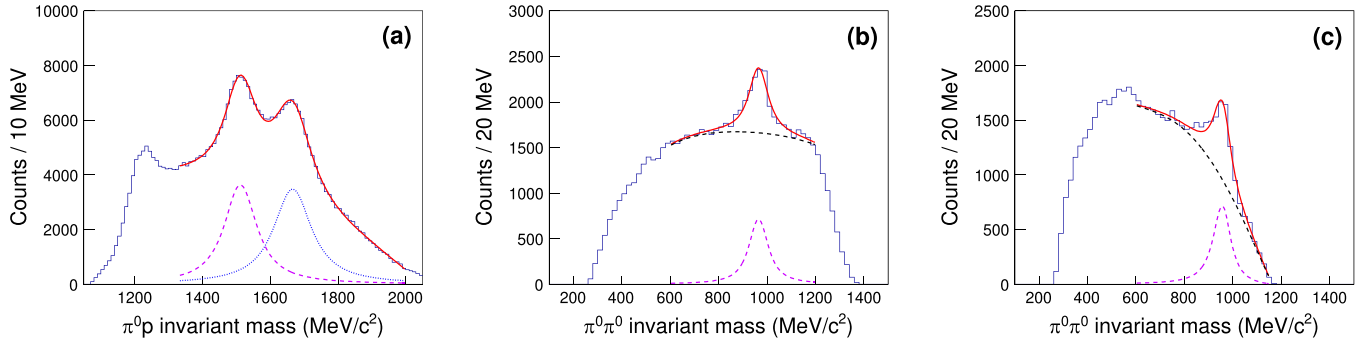


FIG. 1. Invariant mass spectra for (a)  $\pi^0 p$  and (b), (c)  $\pi^0 \pi^0$  pairs in the selected sample. (b) and (c) are plotted for the total energy ranges  $2110 < W < 2320$  and  $1898 < W < 2110$  MeV, respectively. Voigt functions are fitted with polynomial background functions to extract nucleon resonances in (a) and  $f_0(980)$  signals in (b) and (c).

in the signal yield extractions at individual  $f_0(980)$  polar angle bins, where the statistics were limited.

Differential cross sections  $d\sigma/d\Omega$  of the reaction  $\gamma p \rightarrow f_0(980)p \rightarrow \pi^0 \pi^0 p$  were measured in each 0.25 of  $\cos \theta_{f_0}^{c.m.}$  for both the higher and lower  $W$  regions. The  $\pi^0 \pi^0$  invariant mass distribution in the individual kinematic bin was fitted by the prefixed Voigt function (for a signal peak) with a fourth-order polynomial (for backgrounds) in a wide range, typically over an interval of 700–750 MeV/ $c^2$ . Signal yields were obtained by integrating the Voigt function with fitted scale factors. A geometrical acceptance factor of the experimental setup together with most of detection efficiencies was estimated in each kinematic bin by using the MC simulation mentioned above. In this simulation,  $f_0(980)$  mesons were generated with no energy and angular dependence of the reaction rate in the center-of-mass frame. The maximum acceptance value was obtained at the most backward  $f_0(980)$  angles, reaching more than 30%. There was no sufficient acceptance at  $\cos \theta_{f_0}^{c.m.} \gtrsim 0.75$ . Other efficiencies and correction factors, including a photon beam transmittance over the beamline, a reconstruction efficiency of the recoil electron at the tagging detector, a wrong-counting rate of tagged beam photons, discrepancies of proton and  $\gamma$  detection efficiencies in the real and MC data analyses, were derived in the same way as the previous publications [14,16,17]. In addition, the branching fraction of the  $\pi^0 \rightarrow \gamma\gamma$  decay (98.8%) was also taken into account. The branching fraction of  $f_0(980) \rightarrow \pi^0 \pi^0$  decays is not included in the calculation of differential cross sections.

Systematic uncertainties in the cross section measurement mainly arise from the fitting method, where a Voigt function was prefixed for stable fits. For the estimation of such uncertainties, the mass and width of the Voigt function were changed from the standard values in the fits to extract signal yields. Based on the observed deviation between the masses determined in Figs. 1(b) and 1(c), the fixed mass of the Voigt function was varied by  $\pm 10$  MeV/ $c^2$ . In different fits, the width was changed by  $\pm 12$  MeV/ $c^2$ , corresponding to the  $1\sigma$  fitting error in Fig. 1(b). The signal extraction fit was also influenced by a choice of background functions, so that the fourth-order polynomial was replaced to second- and third-order polynomials in additional tests with narrower fitting ranges. Other systematic uncertainties were evaluated in terms

of the photon beam transmittance, the photon beam position, the  $\chi^2$  probability cut in the kinematic fit, and the target length, in the same way as the previous analyses [14,16,17]. The total uncertainties in individual kinematic bins were typically around 15% after taking a quadratic sum. They were dominated by the variation depending on fitting methods, particularly the change of the  $f_0(980)$  mass and width.

Figure 2 shows the differential cross sections measured for wide  $\cos \theta_{f_0}^{c.m.}$  ranges. Two sets of differential cross sections were obtained by using the event selection conditions without (closed circles) and with (open squares) the  $N^*$  cuts. The difference between the two results possibly indicates additional systematic uncertainties arising from the fitting instability by the variation of event selection or the influence

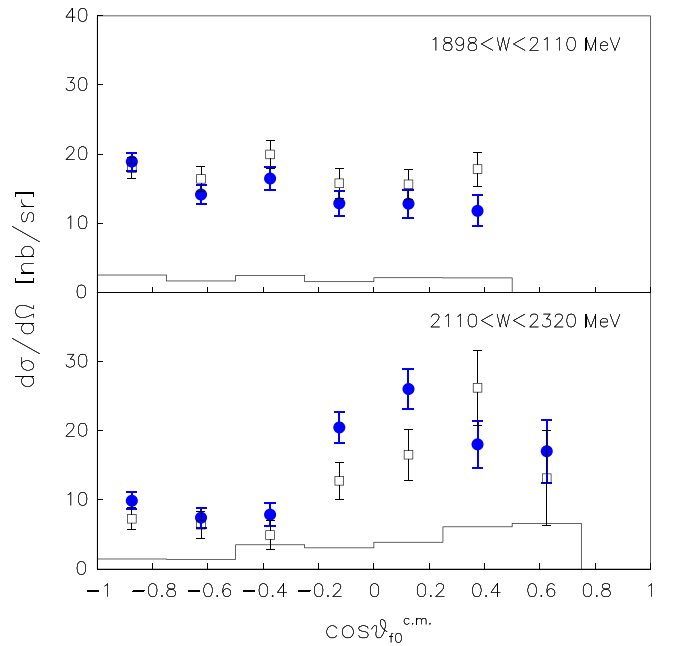


FIG. 2. Differential cross sections  $d\sigma/d\Omega$  of the reaction  $\gamma p \rightarrow f_0(980)p \rightarrow \pi^0 \pi^0 p$  for the two event-selection conditions without (closed circles) and with (open squares) requirement of the  $N^*$  cuts. The vertical bars show statistical uncertainties. The histograms represent the magnitudes of systematic uncertainties for the case without the  $N^*$  cuts.

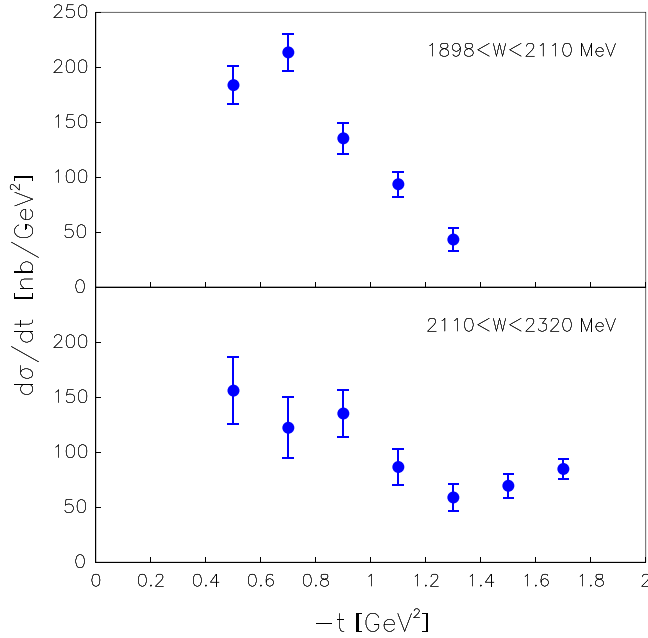


FIG. 3. Differential cross sections  $d\sigma/dt$  of the reaction  $\gamma p \rightarrow f_0(980)p \rightarrow \pi^0\pi^0p$  with no requirement of the  $N^*$  cuts.

of interference with backgrounds, but is modest compared with the evaluated statistical and systematic uncertainties. The polar angle dependence of differential cross sections was nearly flat in the lower  $W$  region. In contrast, an enhancement at  $\cos\theta_{f_0}^{\text{c.m.}} \gtrsim 0$  appeared at the higher total energies, indicating the increase of  $t$ -channel contributions. Because the initial state  $\gamma$  has a vector nature,  $\rho$  and  $\omega$  mesons are expected as exchange particles. The results at lower energies and backward angles may suggest sizable contributions from  $s$ - and  $u$ -channel diagrams, which have not been discussed theoretically.

Differential cross sections  $d\sigma/dt$  were also measured in a similar way as  $d\sigma/d\Omega$  for the comparison of the experimental result with a theoretical prediction. Figure 3 shows the result depending on  $|-t|$  with the intervals of  $0.2 \text{ GeV}^2$ . Only the case without the  $N^*$  cuts was examined because it turned out that their influence was not large in Fig. 2. In the higher  $W$  region, a smaller  $|-t|$  enhancement was observed as expected from  $t$ -channel diagrams. At the lower energies near the production threshold, the  $f_0(980)$  photoproduction is kinematically limited to a smaller  $|-t|$  region. The result at the higher energies shows the  $d\sigma/dt$  of around  $0.1 \mu\text{b}/\text{GeV}^2$  or more for  $|-t| < 1 \text{ GeV}^2$ . This differential cross section is comparable to the prediction in Fig. 4 of Ref. [5], although this theoretical calculation has been done at  $E_\gamma = 3.5 \text{ GeV}$ . A stronger contribution from a  $q\bar{q}$  component in the  $f_0(980)$  meson may be suggested in an interpretation based on a Reggeized model, as described in Ref. [5].

Photon beam asymmetries  $\Sigma$  were measured in the two energy ranges defined above, but with the  $\cos\theta_{f_0}^{\text{c.m.}}$  bins of each 0.50. Signal yield extraction was done by dividing the final sample into the two azimuthal angle ( $\Phi$ ) regions that were perpendicular ( $\pi/4-3/4\pi$  and  $5/4\pi-7/4\pi$ ) and parallel ( $-\pi/4-\pi/4$  and  $3/4\pi-5/4\pi$ ) to the polarization vector of the

photon beam. This coarse binning was adopted because of the statistical reason. For the individual kinematic bins, the sum of a fixed Voigt function and a fourth-order polynomial was fitted to evaluate  $f_0(980)$  signal counts in the perpendicular and parallel regions ( $N_\perp$  and  $N_\parallel$ , respectively), as done in the cross-section measurement. Here,  $N_\perp$  and  $N_\parallel$  correspond to

$$N_\perp = \int_{\pi/4}^{3/4\pi} \frac{d\sigma_0}{d\Omega} (1 - P_\gamma \Sigma \cos 2\Phi) d\Phi + \int_{5/4\pi}^{7/4\pi} \frac{d\sigma_0}{d\Omega} (1 - P_\gamma \Sigma \cos 2\Phi) d\Phi \quad (1)$$

$$N_\parallel = \int_{-\pi/4}^{\pi/4} \frac{d\sigma_0}{d\Omega} (1 - P_\gamma \Sigma \cos 2\Phi) d\Phi + \int_{3/4\pi}^{5/4\pi} \frac{d\sigma_0}{d\Omega} (1 - P_\gamma \Sigma \cos 2\Phi) d\Phi, \quad (2)$$

where  $\frac{d\sigma_0}{d\Omega}$  represents an unpolarized differential cross section. Values of the photon beam polarization  $P_\gamma$  were determined to be 0.677 and 0.895 for the lower and higher  $W$  regions, respectively, based on the calculation using Eq. (16) of Ref. [27]. The  $\Sigma$  was finally obtained by the following equation:

$$P_\gamma \Sigma / f_{\text{int}} = (N_\perp - N_\parallel) / (N_\perp + N_\parallel), \quad (3)$$

where  $f_{\text{int}} = \pi/2$  was a correction factor for the integration over  $\pi/2$  azimuthal angle ranges. Any acceptance correction was not applied to the  $\Sigma$  measurement.

The experimental data were collected by orienting the photon beam polarization vector alternately to the vertical and horizontal directions in the laboratory frame. In the evaluation of  $\Sigma$ s, the two data sets were added after aligning the azimuthal directions of polarization vectors to minimize the systematic uncertainty due to the imperfection of azimuthal symmetry in the detector system. However, the difference of  $\Sigma$ s in the two data sets was conservatively treated as one of systematic uncertainties. Other systematic uncertainties were estimated by considering the sources related to the fitting method in the same way as the differential cross-section measurement. The total uncertainties were typically around 0.15 in the unit of  $\Sigma$ .

Figure 4 shows the measured  $\Sigma$ s in both cases without (closed circles) and with (open squares) the  $N^*$  cuts. The two results are consistent with each other, suggesting that the influence of possible interference is small compared with the statistical and systematic uncertainties. The detector acceptance was limited at the most forward  $f_0(980)$  angles. While the  $\Sigma$ s in the lower  $W$  bin are close to zero or slightly positive, the higher  $W$  region provides negative  $\Sigma$ s around  $-0.3$ . The negative values in the case of scalar-meson photoproduction indicate the contribution of  $t$ -channel vector-meson (natural parity) exchange, as discussed in Ref. [7]. The deviation from  $\Sigma = -1$  can arise not only from the contamination of  $s$ - and  $u$ -channel diagrams but also from the unnatural parity contribution of axial-vector exchange [e.g.,  $b_1(1235)$ ] and rescattering diagrams with two Reggeon exchange [5]. Particularly, the coupling of the  $f_0(980)$  meson



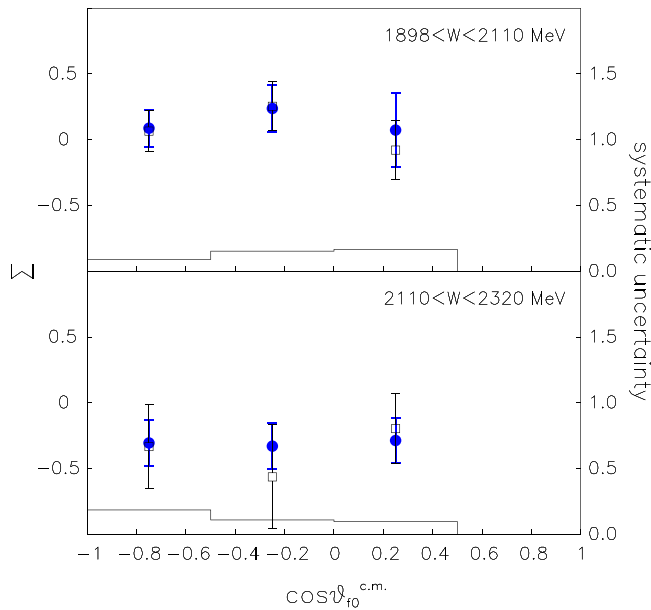


FIG. 4. Photon beam asymmetries  $\Sigma$  of the reaction  $\gamma p \rightarrow f_0(980)p$  for the two event-selection conditions without (closed circles) and with (open squares) requirement of the  $N^*$  cuts. The vertical bars show statistical uncertainties. The histograms represent the magnitudes of systematic uncertainties (right-side scale) for the case without the  $N^*$  cuts.

with the rescattering diagrams may be interesting to explore its structure in future theoretical works.

In summary, differential cross sections and photon beam asymmetries of the reaction  $\gamma p \rightarrow f_0(980)p \rightarrow \pi^0\pi^0 p$  were measured for the first time. A clear peak of the  $f_0(980)$  signal was observed in the  $\pi^0\pi^0$  invariant mass distribution without the influence of vector-meson photoproduction. The differential cross sections indicate the increase of  $t$ -channel contributions at  $E_\gamma \approx 2.1$  GeV. The  $d\sigma/dt$  measured in a smaller  $|-t|$  region is comparable to the theoretical prediction assuming a  $q\bar{q}$  component in  $f_0(980)$ . At  $E_\gamma \approx 2.1$  GeV, photon beam asymmetries  $\Sigma$  provide negative values, which suggest a large contribution of  $t$ -channel vector-meson exchange with influence of other diagrams. The present results will give useful information about the  $f_0(980)$  meson structure.

The experiment was performed at the BL31LEP of SPring-8 with the approval of the Japan Synchrotron Radiation Institute (JASRI) as a contract beamline (Proposal No. BL31LEP/6101). The authors gratefully acknowledge to the support of the staff at SPring-8 for providing excellent experimental conditions. This research was supported in part by the Ministry of Education, Culture, Sports, Science and Technology of Japan, JSPS KAKENHI Grants No. 19002003, No. 24244022, No. 21H04986, and the Ministry of Science and Technology of Taiwan.

- [1] R. L. Workman *et al.* (Particle Data Group), *Prog. Theor. Exp. Phys.* **2022**, 083C01 (2022).
- [2] F. E. Close and N. A. Törnqvist, *J. Phys. G: Nucl. Part. Phys.* **28**, R249 (2002).
- [3] C. Amsler and N. A. Törnqvist, *Phys. Rep.* **389**, 61 (2004).
- [4] E. Klempt and A. Zaitsev, *Phys. Rep.* **454**, 1 (2007).
- [5] A. Donnachie and Yu. S. Kalashnikova, *Phys. Rev. C* **93**, 025203 (2016).
- [6] A. Donnachie and Yu. S. Kalashnikova, *Phys. Rev. C* **78**, 064603 (2008).
- [7] I. I. Strakovsky *et al.*, *Phys. Rev. C* **107**, 015203 (2023).
- [8] C.-R. Ji, R. Kamiński, L. Leśniak, A. Szczepaniak, and R. Williams, *Phys. Rev. C* **58**, 1205 (1998).
- [9] J.-H. Lee, H.-C. Kim, S.-H. Kim, H.-Y. Ryu, and B.-G. Yu, *Prog. Theor. Exp. Phys.* **2017**, 093D05 (2017).
- [10] M. Battaglieri *et al.* (CLAS Collaboration), *Phys. Rev. Lett.* **102**, 102001 (2009).
- [11] S. Chandavar *et al.* (CLAS Collaboration), *Phys. Rev. C* **97**, 025203 (2018).
- [12] N. Muramatsu, M. Yosoi, T. Yorita, Y. Ohashi *et al.*, *Nucl. Instrum. Meth. Phys. Res. A* **1033**, 166677 (2022).
- [13] N. Muramatsu *et al.*, *Nucl. Instrum. Meth. Phys. Res. A* **737**, 184 (2014).
- [14] N. Muramatsu *et al.* (LEPS2/BGOegg Collaboration), *Phys. Rev. C* **100**, 055202 (2019).
- [15] N. Tomida, N. Muramatsu, M. Niiyama *et al.* (LEPS2/BGOegg Collaboration), *Phys. Rev. Lett.* **124**, 202501 (2020).
- [16] N. Muramatsu *et al.* (LEPS2/BGOegg Collaboration), *Phys. Rev. C* **102**, 025201 (2020).
- [17] T. Hashimoto, T. Nam, N. Muramatsu *et al.* (LEPS2/BGOegg Collaboration), *Phys. Rev. C* **106**, 035201 (2022).
- [18] T. Ishikawa *et al.*, *Nucl. Instrum. Meth. Phys. Res. A* **837**, 109 (2016).
- [19] M. Ablikim *et al.* (BESIII Collaboration), *Phys. Rev. D* **92**, 012007 (2015).
- [20] M. Ablikim *et al.* (BESIII Collaboration), *Phys. Rev. Lett.* **108**, 182001 (2012).
- [21] K. M. Ecklund *et al.* (CLEO Collaboration), *Phys. Rev. D* **80**, 052009 (2009).
- [22] S. Uehara, Y. Watanabe *et al.* (Belle Collaboration), *Phys. Rev. D* **78**, 052004 (2008).
- [23] B. Aubert *et al.* (BABAR Collaboration), *Phys. Rev. D* **76**, 012008 (2007).
- [24] S. Flatté, *Phys. Lett. B* **63**, 224 (1976).
- [25] N. N. Achasov and G. N. Shestakov, *Phys. Rev. D* **72**, 013006 (2005); N. N. Achasov and A. V. Kiselev, *ibid.* **68**, 014006 (2003); N. N. Achasov and V. V. Gubin, *ibid.* **63**, 094007 (2001).
- [26] S. Agostinelli *et al.*, *Nucl. Instrum. Meth. Phys. Res. A* **506**, 250 (2003); J. Allison *et al.*, *IEEE Trans. Nucl. Sci.* **53**, 270 (2006); *Nucl. Instrum. Meth. Phys. Res. A* **835**, 186 (2016).
- [27] A. D'Angelo *et al.*, *Nucl. Instrum. Meth. Phys. Res. A* **455**, 1 (2000).